



# Synergy between hydrogen and ceria in Pt-catalyzed CO oxidation: An investigation on Pt–CeO<sub>2</sub> catalysts synthesized by solution combustion



Franck Morfin, Thanh-Son Nguyen, Jean-Luc Rousset, Laurent Piccolo\*

*Institut de recherches sur la catalyse et l'environnement de Lyon (IRCELYON), UMR 5256CNRS & Université Claude Bernard—Lyon 1, 2 avenue Albert Einstein, F-69626 Villeurbanne, France*

## ARTICLE INFO

### Article history:

Received 24 November 2015

Received in revised form 24 January 2016

Accepted 25 January 2016

Available online 27 January 2016

### Keywords:

Ceria

Platinum

CO oxidation

PROX

Solution combustion synthesis

## ABSTRACT

Pt–CeO<sub>2</sub> catalysts were prepared by solution combustion synthesis (SCS), a simple and fast one-pot method, using glycine or oxalyl dihydrazide (ODH) as the fuel and Pt chloride or nitrate as the metal precursor. The samples were characterized by ICP-OES, N<sub>2</sub> volumetry, XRD, XPS, aberration-corrected (S)TEM, CO-DRIFTS and microRaman spectroscopy. The SCS catalysts were evaluated in CO oxidation and preferential oxidation (PROX) of CO in H<sub>2</sub> excess, and compared to Pt/CeO<sub>2</sub> and Pt/Al<sub>2</sub>O<sub>3</sub> catalysts prepared by incipient wetness impregnation. The glycine fuel yields better results than ODH in terms of Pt dispersion and catalytic performance. The fresh Cl-containing catalysts consist of PtO nanoparticles poorly active in CO oxidation, while the catalysts synthesized from Pt nitrate contain highly active Pt<sup>δ+</sup> (0 < δ < 2) species in interaction with ceria. Consistently, the most efficient catalyst for H<sub>2</sub>-free CO oxidation is the one synthesized from glycine and Pt nitrate. For PROX, the selectivity to CO<sub>2</sub> is 100% at low temperature and decreases in a similar way for all the Pt–CeO<sub>2</sub> catalysts above ca. 100 °C. With respect to H<sub>2</sub>-free conditions, the CO PROX activity of the Pt–CeO<sub>2</sub> catalysts is considerably enhanced (activity multiplied by up to 60 at 110 °C), while the activity gain is comparatively minor for Pt/Al<sub>2</sub>O<sub>3</sub>. We conclude that hydrogen, by increasing the mobility of oxygen species at the surface of ceria, promotes the support-assisted pathway of CO oxidation.

© 2016 Elsevier B.V. All rights reserved.

## 1. Introduction

Beyond the prototypical catalytic oxidation of CO, the preferential oxidation of CO in hydrogen excess (PROX) has been suggested as a viable process to remove CO impurities from reformate hydrogen, in order to feed onboard proton-exchange-membrane fuel cells with pure hydrogen and thereby avoid the Pt anode poisoning by CO [1–3]. PROX has been widely studied over platinum-group metals (PGMs, i.e. Pt, Pd, Ir, Rh, Ru, and Os) supported on non-reducible oxides (typically Pt/Al<sub>2</sub>O<sub>3</sub>), and coinage metals supported on reducible oxides (typically CuO/CeO<sub>2</sub>). Conversely, the combination of PGMs with reducible oxides has been much less studied, although reducible oxides are known to act as PGM promoters in PROX [3]. Due to its excellent redox properties, ceria is extensively used in heterogeneous catalysis, where it can act as an oxygen buffer for oxidation reactions [4]. The three-way cat-

alytic converter for gasoline-powered automotive engines is the best known catalytic application of ceria. It typically consists of a monolith washcoated with a ceria-zirconia/alumina film containing Pt, Pd, and Rh nanoparticles, which are active for catalyzing CO/hydrocarbon oxidation and NO<sub>x</sub> reduction. Both for CO oxidation and PROX, ceria has proved its superiority over any other simple oxide as a PGM support, especially at low temperatures [5–7]. This is explained by the existence, in addition to the standard Langmuir–Hinshelwood mechanism which proceeds on the metal only, of a second mechanism involving oxygen from ceria at the metal/ceria interface [5,8].

Combustion synthesis forms a class of relatively simple and inexpensive methods for preparing advanced solid materials, generally (mixed) metal oxides. It relies on the fact that an exothermic reaction can be self-sustained by the heat it generates, i.e. without external energy supply, except for ignition. Depending on the solid, liquid, or gaseous nature of the metal precursor phase, the method is called self-propagating high-temperature synthesis (SHS), solution combustion synthesis (SCS), or flame synthesis, respectively. SCS consists in the fast and self-sustained combustion of a pre-

\* Corresponding author.

E-mail address: [laurent.piccolo@ircelyon.univ-lyon1.fr](mailto:laurent.piccolo@ircelyon.univ-lyon1.fr) (L. Piccolo).

heated aqueous solution of a metallic salt (usually nitrate) and an organic fuel (e.g. urea, glycine, or oxalyl dihydrazide, i.e. ODH). The solid oxide material obtained is generally nanocrystalline, making it suitable for heterogeneous catalysis [9].

The synthesis of oxides loaded with precious metals by combustion is much less conventional. Bera, Hegde and coworkers succeeded in using the SCS method to prepare, in a single step, solid oxides mostly based on  $\text{CeO}_2$  loaded with noble metals [10–13]. Using XRD, XPS and EXAFS, the authors reported the formation of so-called  $\text{Ce}_{1-x}\text{M}_x\text{O}_{2-\delta}$  solid solutions (herein referred to as  $\text{M}-\text{CeO}_2$ ,  $\text{M}$  being the metal). According to the authors, the atomic dispersion of the metals, a large fraction of which would be substituted in the ceria lattice as cations, gives rise to an exceptionally high catalytic activity in such reactions as CO oxidation and NO reduction. SCS was also employed by other groups to prepare Pt, Pd, Rh and Ru nanoparticles supported on ceria or ceria-zirconia for catalyzing various reactions [14–21]. Recently, we synthesized for the first time by combustion Ir– $\text{CeO}_2$  catalysts, which showed high performance in the steam reforming of methane at 750 °C [22,23]. In particular, the high catalyst stability was ascribed to the favorable metal–ceria interaction provided by one-pot SCS. In addition, this fast synthesis method allowed us to compare the performances of ceria-supported platinum-group metals in CO oxidation and PROX [24]. While Rh– $\text{CeO}_2$  appeared as the most efficient catalyst for CO oxidation under our conditions (CO:O<sub>2</sub> = 2:2 mol% of 1 atm), Pt– $\text{CeO}_2$  is the most efficient one in PROX. A further investigation of H<sub>2</sub>-free CO oxidation on both catalysts using operando DRIFTS-MS showed that Pt– $\text{CeO}_2$  becomes superior to Rh– $\text{CeO}_2$  under CO-rich conditions (CO:O<sub>2</sub> = 7:1 mol%) due to the greater versatility of the oxidation state of Pt interacting with ceria [25].

In the present work, the combustion-synthesized Pt– $\text{CeO}_2$  system is selected to investigate in a systematic way the effect of the metal precursor (chloride vs nitrate) and the fuel (glycine vs ODH) on the catalyst structure and CO oxidation/PROX performance. In addition, Pt– $\text{CeO}_2$  is compared to pristine  $\text{CeO}_2$ , as well as to Pt/CeO<sub>2</sub> and Pt/Al<sub>2</sub>O<sub>3</sub> catalysts prepared by conventional incipient wetness impregnation. Along with extensive microscopic and spectroscopic investigations, this allows us to gain insight into the active state of platinum and the mechanism of PROX on Pt/CeO<sub>2</sub>.

## 2. Experimental

### 2.1. Catalyst preparation

A series of  $\text{CeO}_2$  and Pt– $\text{CeO}_2$  powders (see Table 1) was prepared by solution combustion synthesis (SCS), using ceric ammonium nitrate, CAN [(NH<sub>4</sub>)<sub>2</sub>Ce(NO<sub>3</sub>)<sub>6</sub>, Sigma-Aldrich, 99.99%] as both ceria precursor salt and oxidizing agent. The Pt precursors were chloroplatinic acid (H<sub>2</sub>PtCl<sub>6</sub>·6H<sub>2</sub>O, Strem Chemicals, 38–40% Pt) or tetra-ammine platinum(II) nitrate (Pt(NH<sub>3</sub>)<sub>4</sub>(NO<sub>3</sub>)<sub>2</sub>, Sigma-Aldrich, >50% Pt). Glycine (C<sub>2</sub>H<sub>5</sub>NO<sub>2</sub>, Sigma-Aldrich, 99%) or oxalyl dihydrazide (ODH, C<sub>2</sub>H<sub>6</sub>N<sub>4</sub>O<sub>2</sub>, Sigma-Aldrich, 98%) were used as fuels. The CAN:fuel:Pt precursor mixture composition was chosen in order to obtain stoichiometric proportions of oxidizer and fuel (i.e., with the oxidizing/reducing valence ratio of the redox mixture  $\varphi = 1$  [26]) and reach the desired metal loading (generally 1 wt%). Table 1 shows the actual loadings.

Practically, a borosilicate beaker (300 cm<sup>3</sup>) containing a mixture of CAN (5.00 g), glycine (1.82 g) or ODH (2.56 g), Pt precursor (95 mg), and 30 mL deionized water was introduced into a muffle furnace (Carbolite ELF 11/6) maintained at 350 °C. At the point of complete dehydration (5–10 min), the solution started boiling and foaming, and ignition took place after a few seconds with rapid evolution of a large quantity of gases. This yielded a voluminous solid

product within a few minutes. The powder color ranged from pale yellow ( $\text{CeO}_2$ ) to brown-grey (Pt– $\text{CeO}_2$ ).

After combustion synthesis, the samples were in an oxidized state [25]. A standard *ex situ* reducing treatment consisting in heating the as-prepared samples to 400 °C (5 °C min<sup>-1</sup>, 2 h plateau) in pure H<sub>2</sub> flow (3–7 L h<sup>-1</sup>, 1 atm), was applied before some of the microscopy and Raman analyses. For XPS and FTIR, a similar treatment could be applied *in situ* (see next subsection). The reduction temperature (400 °C) was chosen similar to the maximum temperature (ca. 370 °C) reached in our PROX experiments (which are performed in large H<sub>2</sub> excess). As will be shown in Section 3.2, a reduction at higher temperature was attempted, but did not further affect the catalyst activity.

For preparing a reference impregnated catalyst (Pt/CeO<sub>2</sub>-IWI), platinum was deposited by incipient wetness impregnation (IWI) of H<sub>2</sub>PtCl<sub>6</sub>·6H<sub>2</sub>O over pristine  $\text{CeO}_2$  prepared by SCS using glycine. The support (1 g) was impregnated with an appropriate amount of the aqueous solution of Pt precursor (26.3 mg), corresponding to the support pore volume. The sample was matured for 2 h at ambient temperature and dried overnight at 110 °C, then calcined at 500 °C in air flow for 2 h, and finally reduced at 400 °C in H<sub>2</sub> flow for 2 h.

### 2.2. Catalyst characterization

The metal amounts were determined by inductively coupled plasma–optical emission spectroscopy (ICP-OES, Activa instrument from Horiba Jobin Yvon). In order to dissolve them completely, the samples were treated with a mixture of H<sub>2</sub>SO<sub>4</sub>, aqua regia and HF at 250–300 °C.

Specific surface areas were derived from N<sub>2</sub> adsorption volumetry at –196 °C (ASAP 2010 M instrument from Micromeritics) using the BET method. Prior to the measurements, the powders were outgassed at 300 °C for 2 h in vacuum.

The crystalline structure of the powders was analyzed at RT and ambient atmosphere using a Bruker D8 Advance A25 X-ray diffractometer (Cu K $\alpha$  radiation at 0.154184 nm) equipped with Ni filter and 1-D fast multistrip detector (LynxEye, 192 channels on 2.95°). The diffractograms were collected at 2 $\theta$  with steps of 0.02° from 20 to 85° for a total acquisition time of 110 min. Phase identification was performed using the Diffrac. Eva software (Bruker) and the ICDD-PDF4+ database. The lattice parameters and the crystallite sizes were determined using the Rietveld method (Fullprof code).

X-ray photoelectron spectroscopy (XPS) was carried out with a KRATOS AXIS Ultra DLD spectrometer using a monochromated Al K $\alpha$  X-ray source (1486.6 eV). The spectra were referenced to the 3d<sub>3/2</sub> peak of Ce<sup>4+</sup> at 916.0 eV binding energy. Before surface analysis, the samples could be heated to 400 °C for 2 h under H<sub>2</sub> flow (50 mL min<sup>-1</sup>, 1 atm) in an *in situ* high-temperature quartz reaction cell. For determining Ce<sup>3+</sup>/Ce<sup>4+</sup> ratios from the Ce 3d core levels, a fitting procedure using a linear combination of spectra obtained for our own  $\text{CeO}_2$  and  $\text{Ce}_2\text{O}_3$  samples was employed [22].

The sample microstructure was imaged through high-resolution transmission electron microscopy (TEM) using a Jeol JEM-2010 operating at 200 kV (images of Fig. S4 Supporting information), and TEM (Fig. S5) or scanning transmission electron microscopy–high angle annular dark field (STEM-HAADF, Fig. 2) using a FEI Titan G2 aberration-corrected ETEM (in high-vacuum mode) operated at 300 kV. For TEM observation, the samples were crushed in ethanol and the solution was ultrasonically stirred before dropping it on a holey carbon-covered copper TEM grid, followed by drying.

The SEM images of Fig. 1 and Fig. S3 were obtained from FEI/Philips ESEM XL-30 (FEG, 3.5 nm resolution at 30 kV operating voltage) and Jeol JSM 5800LV (W filament, 3.5 nm resolution at 15 kV) microscopes, respectively. For sample preparation, the powders were poured as thin layers on double-sided adhesive car-

**Table 1**

Structural characteristics of the samples.

Sample name <sup>a</sup>	P <sub>rep.</sub> method <sup>b</sup>	Pt (wt%) <sup>c</sup>	Cl (wt%) <sup>c</sup>	$d_{\text{Pt}} (\text{nm})/\langle d_{\text{Pt}} \rangle_{\text{surf}}^{\text{d}}$	$d_{\text{CeO}_2} (\text{nm})^{\text{e}}$	$a_{\text{CeO}_2} (\text{\AA})^{\text{e}}$	$S_{\text{BET}} (\text{m}^2/\text{g})^{\text{f}}$
Pt/ $\gamma$ -Al <sub>2</sub> O <sub>3</sub>	IWI	0.95	0.03	$4.3 \pm 1.7/5.7 \text{ nm}$	–	–	ND <sup>g</sup>
CeO <sub>2</sub> (Gly)	SCS	–	–	–	50	5.4123	22
CeO <sub>2</sub> (ODH)	SCS	–	–	–	35	5.4126	12
Pt/CeO <sub>2</sub> IWI (Gly-Cl)	SCS + IWI	1.00	0.63	$1.9 \pm 1.2/3.6 \text{ nm}$	24	5.4134	28
Pt–CeO <sub>2</sub> Gly-Cl	SCS	0.98	0.30	$4.0 \pm 1.3/4.9 \text{ nm}$	27	5.4123	17
Pt–CeO <sub>2</sub> Gly-Cl-w	SCS	0.98	0.10	$3.3 \pm 0.9/3.8 \text{ nm}$	27	5.4123	17
Pt–CeO <sub>2</sub> ODH-Cl	SCS	0.99	0.53	$3.6 \pm 2.0/6.2 \text{ nm}$	9	5.4190	54
Pt–CeO <sub>2</sub> Gly-N	SCS	1.14	–	$4.2 \pm 1.0/4.7 \text{ nm}$	28	5.4142	47
Pt–CeO <sub>2</sub> ODH-N	SCS	1.06	–	$6.8 \pm 3.8/11 \text{ nm}$	73	5.4123	5

<sup>a</sup> In the sample names, Cl and N stand for H<sub>2</sub>PtCl<sub>6</sub>·6H<sub>2</sub>O and Pt(NH<sub>3</sub>)<sub>4</sub>(NO<sub>3</sub>)<sub>2</sub> metal precursors, respectively. Gly and ODH stand for glycine and oxalyl dihydrazide fuel, respectively. The Pt–CeO<sub>2</sub> Gly-Cl-w sample is the washed version of standard Gly-Cl sample. The Pt/ $\gamma$ -Al<sub>2</sub>O<sub>3</sub> sample was purchased from Sigma-Aldrich (product #205966).

<sup>b</sup> IWI and SCS stand for incipient wetness impregnation and solution combustion synthesis, respectively.

<sup>c</sup> Elemental amounts determined by ICP-OES for fresh samples.

<sup>d</sup> Mean Pt particle diameter and standard deviation determined from TEM on the samples pretreated in H<sub>2</sub> flow at 400 °C (except for Gly-Cl-w, fresh sample).  $\langle d_{\text{Pt}} \rangle_{\text{surf}}$  is the Sauter diameter used for TOF calculations.

<sup>e</sup> Mean ceria crystallite size ( $d_{\text{CeO}_2}$ ) and lattice parameter ( $a_{\text{CeO}_2}$ ) determined from XRD Rietveld refinements for fresh samples. The standard deviation on  $a_{\text{CeO}_2}$  is  $\pm 0.0001 \text{\AA}$ .

<sup>f</sup> Specific surface area determined by N<sub>2</sub> adsorption volumetry for fresh samples (BET).

<sup>g</sup> Not determined.

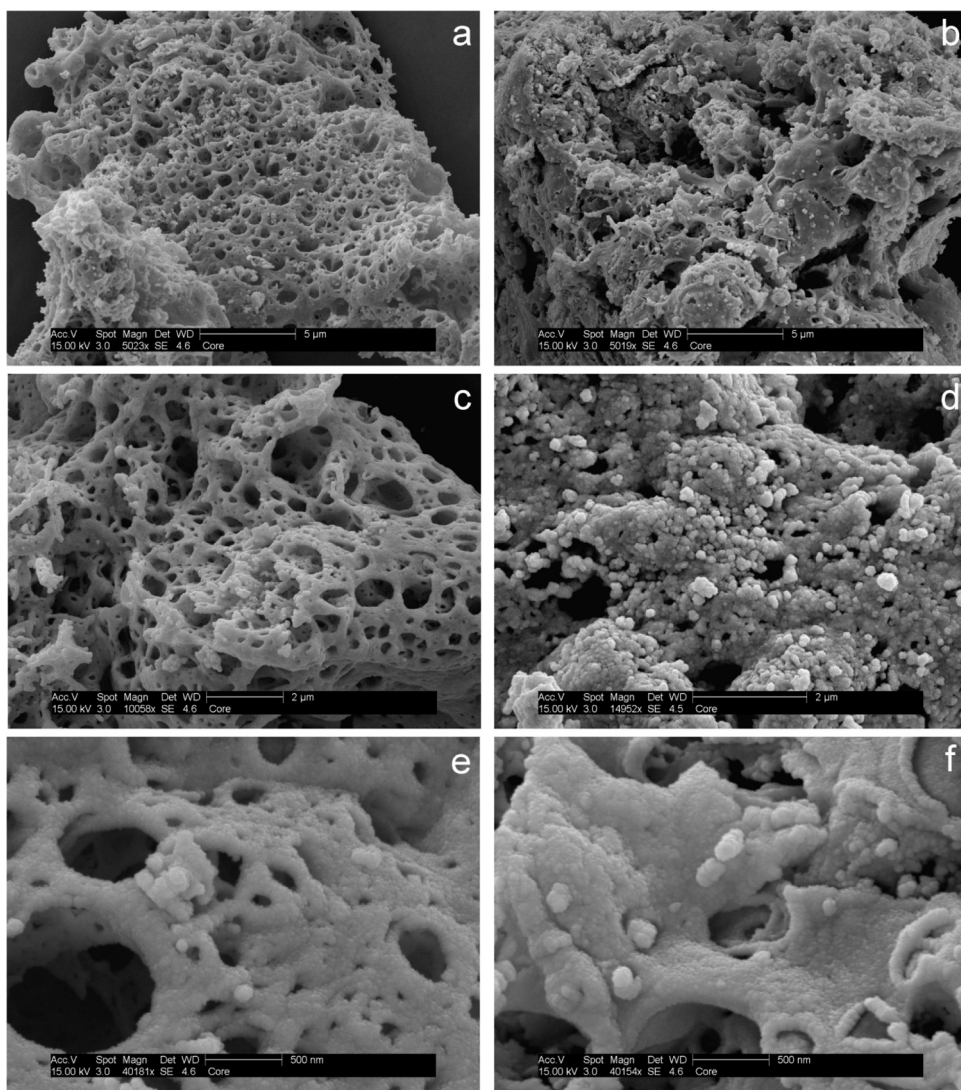


**Fig. 1.** SEM images at 3 different scales for Gly-N (a, c, e) and ODH-N (b, d, f) Pt–CeO<sub>2</sub> samples.

bon discs on the sample holder, and metalized with gold to avoid charging.

Raman spectra of the samples were recorded with a LabRam HR Raman spectrometer (Horiba-Jobin Yvon) equipped with BXFM

confocal microscope, interference and Edge filters, and charge-coupled device detector. The exciting line at 514.5 nm of an argon laser (CVI Melles Griot) was focused using a  $\times 50$  long-working-distance objective. The spectra collected using diffraction grating

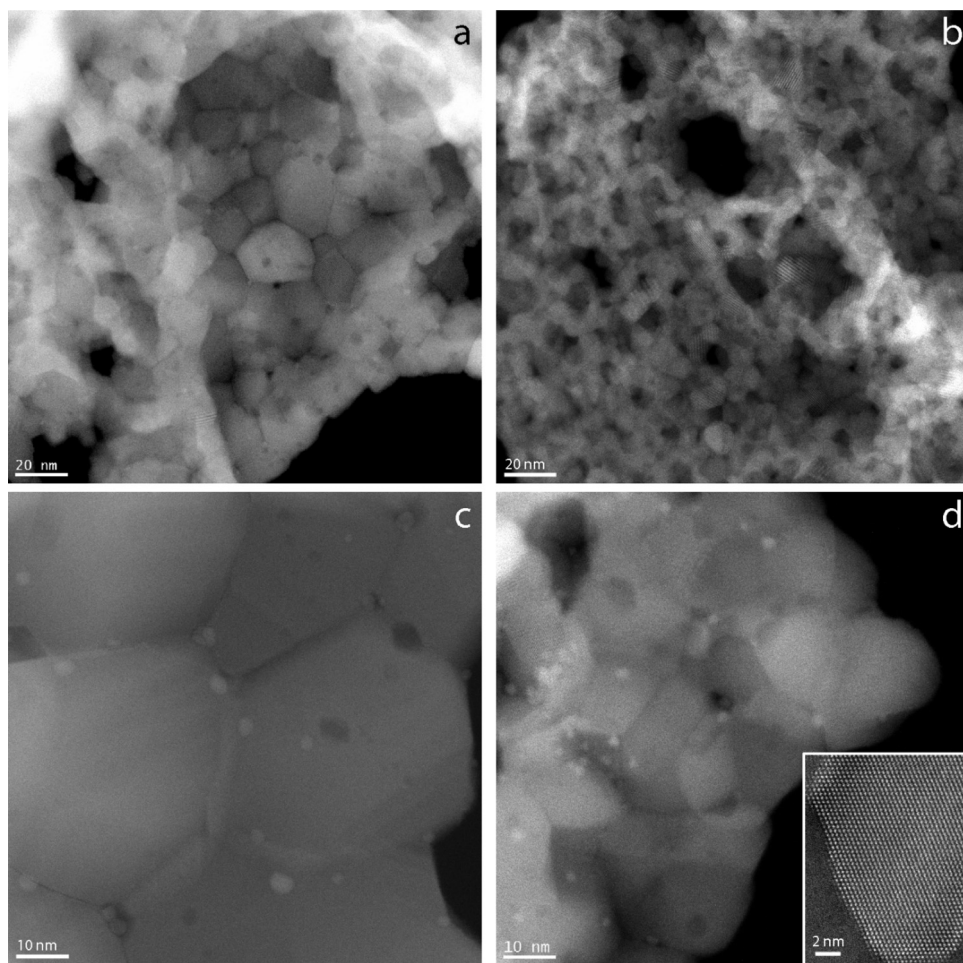


**Fig. 2.** STEM-HAADF images of fresh Pt–CeO<sub>2</sub> Gly-Cl-w (a,c) and ODH-Cl (b, d) samples. The insert of fig. d shows a high-resolution image of a ceria grain in the <0 1 1> direction. The bright spots in figures c and d correspond to Pt nanoparticles, while large dark spots are holes in ceria.

of 1800 grooves per mm were accurate within 1 cm<sup>−1</sup>. Typical Raman spectral collection times were 80 s (20 s per scan and 4 scans per spectrum). The Raman spectra were calibrated using the Si 521 cm<sup>−1</sup> shift, and normalized over the main peak area. All the recorded data were initially treated using the LabSpec software (Horiba-Jobin Yvon).

Infrared spectroscopy of adsorbed CO was performed using a Thermo Nicolet 6700 FTIR spectrophotometer equipped with an *in situ* diffuse reflectance infrared Fourier Transform spectroscopy (DRIFTS) chamber (Harrick HVC-DRP cell) and a high-sensitivity MCT detector. The cell was connected to a gas handling system allowing for *in situ* treatments with several gases at temperatures up to 500 °C. About 30 mg of the powder sample was placed into the cell sample holder and pretreated under He flow (40 mL min<sup>−1</sup>, 1 atm) at 300 °C for 1 h. CO was pre-adsorbed by exposing the sample kept at 50 °C to a flow of 1% CO in He for 15 min. Then the CO + He feed was replaced with pure He, and a spectrum was acquired at 50 °C. For *in situ* reduction, the sample was exposed to a flow of pure H<sub>2</sub> at 400 °C for 1 h. The spectra were recorded in the 650–4000 cm<sup>−1</sup> range at a resolution of 2 cm<sup>−1</sup> by accumulating 128 scans. The Omnic software (Thermo) was used for initial data processing.

### 2.3. Catalyst evaluation

Each catalyst was evaluated in two reactions: the oxidation of CO and the preferential oxidation of CO in H<sub>2</sub> excess (PROX).

These tests were carried out at atmospheric pressure and variable temperature in a continuous flow fixed-bed reactor. The catalysts (about 16 mg) were diluted in Al<sub>2</sub>O<sub>3</sub> (Condea Puralox ScFa-215) in order to obtain a catalytic bed of 800 mg (13 mm height in a quartz U-shaped 10 mm-diameter tubular reactor). The reactant gases were mixed using mass-flow controllers (Brooks Instruments) and flowed through the reactor at a total rate of 50 NmL min<sup>−1</sup>. All the high-purity (>99.995%) gases were purchased from Air Liquide. The gas mixture consisted of 2% CO + 2% O<sub>2</sub> + 96% He for CO oxidation, and 2% CO + 2% O<sub>2</sub> + 48% H<sub>2</sub> + 48% He for PROX. The outlet gases were analyzed online using a Varian MicroGC (CP2003).

The following standard test sequence was used (unless specified) for the catalytic tests: CO oxidation, *in situ* reducing treatment, CO oxidation, and PROX. The pretreatment consisted in heating the catalyst under hydrogen flow (50 mL min<sup>−1</sup>) from room temperature (RT) to 400 °C at a rate of 3 °C min<sup>−1</sup>, followed by 2 h plateau at 400 °C. The CO oxidation and PROX experiments consisted of two heating–cooling cycles (50–350–50 °C) at a rate of 80 °C h<sup>−1</sup>.

## 3. Results

A series of 1 wt% Pt–CeO<sub>2</sub> samples was prepared by solution combustion synthesis (SCS) using chloride or nitrate salt as Pt precursor, and glycine or ODH as fuel. The sample names and main characteristics are reported in Table 1. A catalyst synthesized with chloride salt was washed with distilled water (Gly-Cl-w sample) in order to determine the effect of residual chloride on catalytic

performance. This treatment decreased the Cl amount by a factor of 3 (it cannot be excluded that residual Cl was trapped in the ceria bulk). For comparison, pure  $\text{CeO}_2$  (synthesized by combustion using glycine) and the same type of  $\text{CeO}_2$  impregnated with Pt (IWI sample) were also prepared, and a Pt/ $\text{Al}_2\text{O}_3$  catalyst was used as ceria-free reference.

### 3.1. Characterization

#### 3.1.1. $\text{N}_2$ volumetry

The BET specific surface areas vary in the range 5–54  $\text{m}^2/\text{g}$  (Table 1). The combination of Pt nitrate salt and ODH fuel appears detrimental to the surface area (5  $\text{m}^2/\text{g}$  for the ODH-N sample), whilst the independent use of nitrate or ODH leads to the largest surface areas (54 and 47  $\text{m}^2/\text{g}$  for ODH-Cl and Gly-N samples, respectively). This can be discussed in terms of reaction enthalpies and amounts of evolved gases (see Supporting information, ESI, for details) [9,20,26]. According to the theory of chemical propellants, the SCS reaction releases the maximum energy at a stoichiometric fuel-oxidizer composition ( $\varphi = 1$ , as in our case), leading to a swift temperature rise. If the flame temperature is too high, the solid products agglomerate and consequently exhibit large crystallites and small surface areas. The absolute enthalpy of reaction with ODH is higher than with Gly, especially when ODH is combined with the nitrate precursor ( $-\Delta H = 717 \text{ kcal/mol}$  for ODH-N vs. 540 kcal/mol for ODH-Cl, 452 kcal/mol for Gly-N, and 444 kcal/mol for Gly-Cl). The larger amount of gases evolved in the ODH case (26 mol/mol  $\text{CeO}_2$ ) as compared to the Gly case (21 mol/mol  $\text{CeO}_2$ ) may be instead the key factor explaining the higher dispersion of the ODH-Cl sample as compared to Gly-Cl and Gly-N ones.

The  $\text{N}_2$  physisorption isotherms, as those shown in Fig. S1 (ESI) for  $\text{CeO}_2$  synthesized using glycine or ODH fuel, are intermediate between type IV and type II with a H3 hysteresis loop characteristic of mesoporous materials with a broad pore size distribution that continues into the macropore domain [27]. Moreover, in any case, we can also note the presence of some microporosity. On the opposite, the quasi vertical parallel branches of the loop at high  $\text{N}_2$  pressure can be attributed to the presence of a significant outer surface.

#### 3.1.2. X-ray diffraction

The X-ray diffractograms (Fig. S2) of all the SCS-prepared materials exhibited the fluorite structure of standard  $\text{CeO}_2$  (space group  $Fm-3m$ , #225) [22,24]. The Pt phase was not discernable in the diffractograms recorded in ambient conditions. The ODH-Cl and Gly-N catalysts exhibit larger lattice parameters than the other samples, including pure ceria (Table 1). The variations in the ceria lattice parameter are ascribed to the preparation condition-dependent reduction of  $\text{CeO}_2$ , *i.e.* the above samples have the highest concentrations of  $\text{Ce}^{3+}$  cations (which are larger than  $\text{Ce}^{4+}$  cations, ionic radius 1.14 Å vs. 0.97 Å for coordination 8) due to the formation of oxygen vacancies allowing for charge compensation [28]. This is consistent with the results of Raman spectroscopy (see Fig. 3b and Section 3.1.4 below). However, according to the changes in the lattice parameters with respect to stoichiometric  $\text{CeO}_2$ , the  $\text{Ce}^{3+}/\text{Ce}^{4+}$  ratio is always lower than 2%, which is the estimated value [29] for the ODH-Cl sample. Besides, although the substitution of Ce by Pt has been reported by others [11], this phenomenon cannot be proved (nor excluded) on the basis of our XRD data, since it should involve lattice contraction due to the smaller radius of Pt ions (0.8 Å for  $\text{Pt}^{2+}$  and 0.62 Å for  $\text{Pt}^{4+}$ ) [24].

#### 3.1.3. Electron microscopy

Fig. 1 shows SEM images of two samples prepared either with glycine (left panel) or ODH (right panel) fuel, both using Pt nitrate precursor. It is seen that Gly-N and ODH-N samples exhibit sub-

stantially different textures. Conversely, from the comparison with Fig. S3 showing SEM images of Gly-Cl and ODH-Cl samples, it is concluded that the nature of the Pt precursor (chloride or nitrate) has no visible influence on the structure. The use of glycine leads to a sponge or lace-like morphology [22,23], whereas ODH samples show a cauliflower-like structure (particularly evident on the image of Fig. S3d). However, large round macropores are seen on both types of materials.

Z-contrast STEM images of samples prepared using Pt chloride precursor and glycine or ODH fuel are shown in Fig. 2, while TEM images of the Pt nitrate counterparts are shown in Fig. S4. In addition, Fig. S5 shows HRTEM images of the sample prepared by IWI of Pt on combustion-synthesized ceria. As we previously reported from HRTEM observations [22–25], the use of glycine leads to a puzzle-like structure (Fig. 2(a,c), Fig. S4(a,c), and Fig. S5). Polyhedral pits are frequently observed in the ceria grains (see *e.g.* Fig. S5a). Pt nanoparticles are clearly visible in Fig. 2(c,d), Figs. S4 and S5. Except for the ODH-N sample [Fig. S4(b,d)] which contains relatively large Pt particles (average diameter 7 nm) with large size dispersion (standard deviation 4 nm), the particle size is always 3–4 nm (see Table 1 and size histograms in Fig. S6).<sup>1</sup>

#### 3.1.4. MicroRaman spectroscopy

Examples of Raman spectra for as-prepared  $\text{CeO}_2$  and Pt- $\text{CeO}_2$  SCS samples in the range 200–1800  $\text{cm}^{-1}$  are shown in Fig. 3a. They exhibit an intense band corresponding to the triply degenerate  $F_{2g}$  mode of  $\text{CeO}_2$  with fluorite structure (space group  $O_h^5$ ) [30–33]. This peak is centered at 463  $\text{cm}^{-1}$  for the Pt-containing sample, versus 466  $\text{cm}^{-1}$  for pristine  $\text{CeO}_2$ . The red-shift is attributed to weaker force constants of Ce–O bonds associated with the larger lattice parameter of Pt- $\text{CeO}_2$  (5.4142 vs. 5.4123 Å, see Table 1).

In Fig. 3b, a correlation between the peak full width at half-maximum (FWHM) and its position is clearly visible: the higher the red-shift, the broader the band. The broadening is ascribed to the presence of  $\text{Ce}^{3+}$  cations and oxygen vacancies within the  $\text{CeO}_2$  lattice, which induce disorder and decrease the bond strength [34–36]. For Pt- $\text{CeO}_2$  ODH-N and Gly-N samples, the smaller wavenumber and larger FWHM thus correspond to an increased number of defects. For the Pt- $\text{CeO}_2$  ODH-Cl sample, which exhibits smaller ceria crystallites (9 nm, see Table 1), the broadening could also arise from higher phonon confinement in  $\text{CeO}_2$  nanoparticles [30,32,37], and corresponds to a larger lattice parameter.

Fig. 3c focuses on the region located around the bottom of the main Raman peak (300–1000  $\text{cm}^{-1}$  range). A strong band at 686–689  $\text{cm}^{-1}$ , ascribed to Pt–O vibration [38], is visible for Gly-Cl and ODH-Cl samples, while it is absent for IWI, Gly-N and ODH-N samples. As the Raman response of metal oxides is strongly sensitive to their crystallinity and stoichiometry [38,40,41], Gly-N and ODH-N, which exhibit a broad band between 500 and 750  $\text{cm}^{-1}$ , might form sub-stoichiometric Pt oxides unlike Gly-Cl and ODH-Cl, which most probably contain the stoichiometric  $\text{Pt}(\text{II})\text{O}$  phase [42,43]. Logically, the reducing treatment leads to the disappearance of the 689  $\text{cm}^{-1}$  band (visible for Pt- $\text{CeO}_2$  Gly-Cl in the figure). No Pt oxide is expected in the case of the IWI sample, since its preparation ends with a reduction.

In addition, two peaks at 548  $\text{cm}^{-1}$  and 591  $\text{cm}^{-1}$  are present in the case of the Gly-Cl catalyst. These features appear convoluted for ODH-Cl and ODH-N, and indiscernible from the 500–750  $\text{cm}^{-1}$  band in the other cases. The feature at 548  $\text{cm}^{-1}$  is assigned to Pt–O–Ce vibration, *i.e.* to Pt- $\text{CeO}_2$  interaction [38,39], while the feature at 591  $\text{cm}^{-1}$  is attributed to oxygen vacancies [33]. For Gly-N and IWI,

<sup>1</sup> The significant fraction of big particles in the ODH samples leads to wide or multimodal particle size distributions, with surface-averaged (Sauter) diameters consequently superior to number-averaged ones.

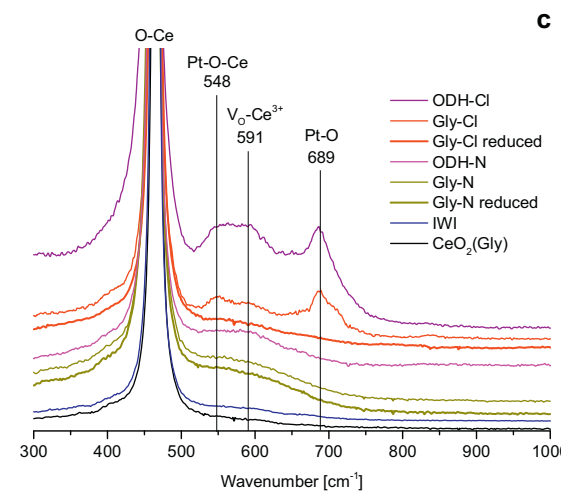
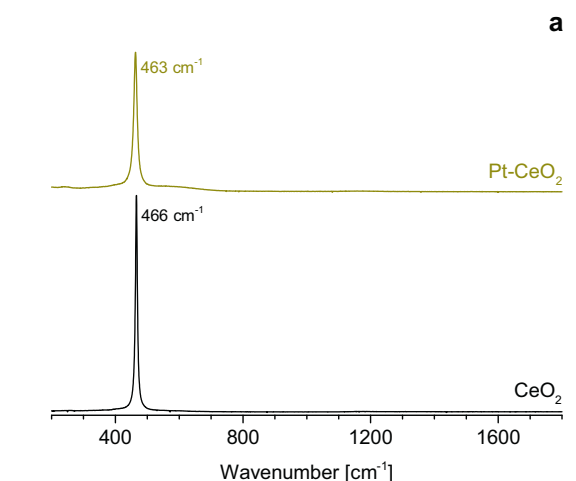


**Fig. 3.** (a) Normalized Raman spectra for fresh  $\text{CeO}_2$  (Gly sample) and  $\text{Pt}-\text{CeO}_2$  (Gly-N sample). (b) Full width at half-maximum versus position of the main Raman peak. (c) Normalized Raman spectra for all fresh and *ex situ* reduced  $\text{CeO}_2$  and  $\text{Pt}-\text{CeO}_2$  samples.

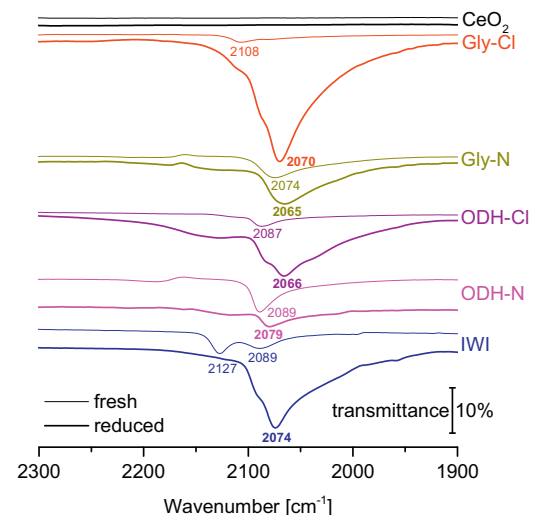


**Fig. 4.** DRIFTS spectra of adsorbed CO measured at 50 °C on fresh and *in situ* reduced  $\text{CeO}_2$  (Gly) and  $\text{Pt}-\text{CeO}_2$  samples.

no distinct peaks are seen, however the continuous band observed in the sole case of Gly-N suggests a larger Pt-*ceria* interface in the SCS sample as compared to the impregnated one. Finally, the partial oxidation of Pt in Gly-N and ODH-N samples might arise from Pt interaction with ceria only, as supported by the predominance of the signal around 500  $\text{cm}^{-1}$  in these cases.

The generally greater oxidation of Pt in the samples prepared using chloride as compared to those prepared with nitrate, as attested by the strong Raman band at 689  $\text{cm}^{-1}$  observed for Gly-Cl and ODH-Cl samples, is tentatively ascribed to the greater stability of the  $\text{Pt}(\text{NH}_3)_4(\text{NO}_3)_2$  complex with respect to the  $\text{H}_2\text{PtCl}_6$  salt. While the latter readily decomposes in water, the former requires a temperature as high as *ca.* 300 °C to fully decompose and subsequently form Pt–O bonds [44].

### 3.1.5. Infrared spectroscopy

In order to determine the nature of the surface adsorption sites and the effect of the reducing pretreatment (400 °C,  $\text{H}_2$  flow), as-prepared and *in situ* reduced materials were characterized by CO-DRIFTS at 50 °C under He flow, after exposure to 1% CO + He flow. The results are presented in Fig. 4.

Bare ceria only presents bands associated to carbonates and formates in the 1300–1600  $\text{cm}^{-1}$  range [25] (not shown). Overall, the fresh Pt catalysts adsorb CO in smaller amounts than the reduced ones. For the fresh samples, a C–O stretching vibration band centered at 2074–2089  $\text{cm}^{-1}$  is generally observed. It is ascribed to CO linearly adsorbed on  $\text{Pt}^0$  [45–48]. In the case of the impregnated sample,  $\text{Pt}-\text{CeO}_2$  IWI, an additional strong band is present at higher wavenumber, 2127  $\text{cm}^{-1}$ , which can be assigned to CO adsorbed on oxidized Pt atoms. For  $\text{Pt}-\text{CeO}_2$  Gly-Cl, the small band at 2108  $\text{cm}^{-1}$ , together with the shoulder at the same wavenumber for the reduced sample, was previously ascribed to CO adsorption on Pt oxide [24]. The CO- $\text{Pt}^0$  band is shifted to lower wavenumbers, 2065–2079  $\text{cm}^{-1}$ , upon reduction. In all cases, the presence of shoulders and tails around the main peak shows the coexistence of a variety of Pt particle surface sites (terraces, facets, edges, etc.). Fig. S7 shows a comparison of the normalized spectra for reduced  $\text{Pt}-\text{CeO}_2$  samples. As a result, the shapes of the main peak are very similar, the essential difference lying in the high-frequency shoulder, which varies in shape and position (from 2117 to 2127  $\text{cm}^{-1}$ ). As it corresponds to CO adsorption on Pt atoms with positive oxidation degree and is more prominent in the cases of the two catalysts

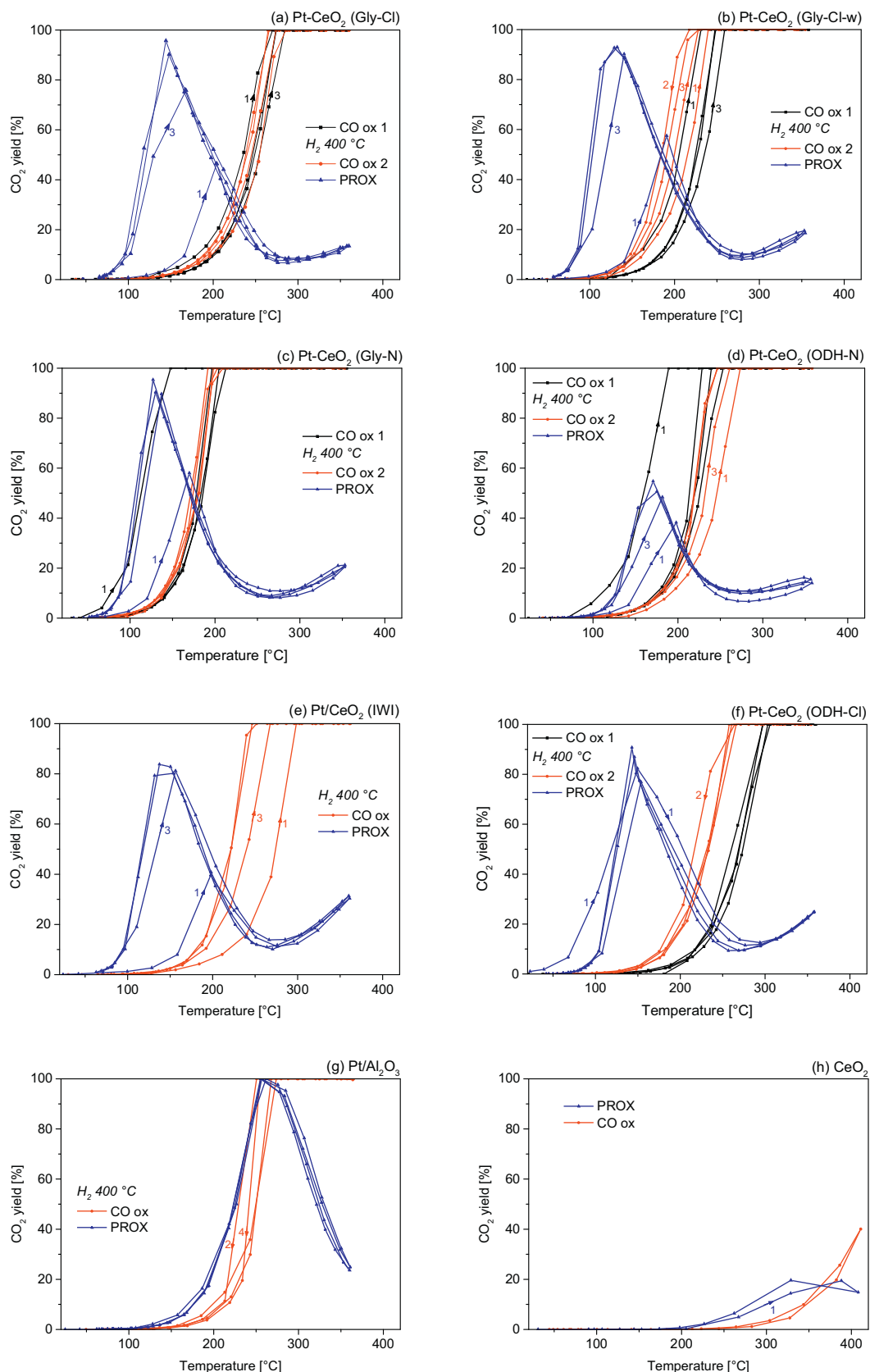


**Fig. 5.** Results of the CO oxidation/PROX experiments. The catalysts in a-d, f and h were first tested as-prepared, while those in e and g were directly pretreated in H<sub>2</sub> flow at 400 °C. The catalyst in h was not pretreated and was first tested in PROX, then in CO oxidation.

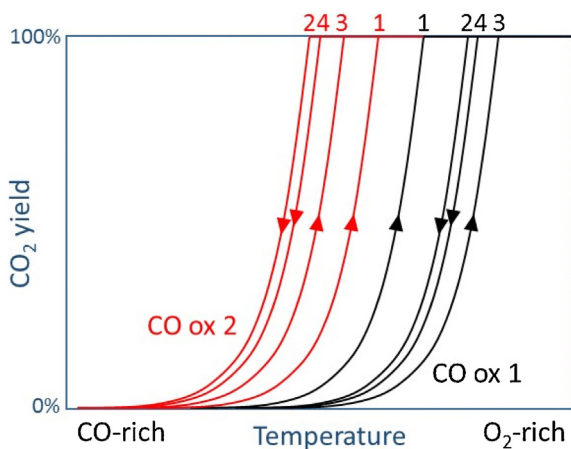


**Fig. 6.** Illustration of the experimental protocol of the CO oxidation experiments. “CO ox 1” and “CO ox 2” series are separated by a reducing treatment. The obtained order of the reaction runs within a series is respected. The two series are represented separately for clarity.

synthesized with ODH, the interaction of Pt with ceria could be stronger for these samples.

Although the DRIFTS technique is hardly quantitative, semi-quantitative comparisons between as-prepared and reduced states can be made for a given sample. Noticeably, the IR bands for the fresh samples prepared using chloroplatinic acid (Gly-Cl and ODH-Cl) are extremely small as compared to their *in situ* pre-reduced counterparts. Conversely, the bands for the fresh samples prepared using tetra-ammine platinum nitrate are almost as intense (Gly-N) or more intense (ODH-N) than those measured for the reduced samples. This suggests that the oxidized Pt phase contained in the fresh Gly-Cl and ODH-Cl catalysts is poorly reactive toward CO adsorption. Interestingly, these samples are the only ones presenting a well-structured Raman peak at 686–689 cm<sup>-1</sup> (Fig. 3c) ascribed to Pt(II) oxide. Thus, it is concluded that partially oxidized Pt (Pt<sup>δ+</sup>, 0 < δ < 2) is more reactive to CO than PtO. The consequences of this conclusion on CO oxidation properties will be shown in the next section.<sup>2</sup>

### 3.2. Catalysis

#### 3.2.1. Cycling behavior in H<sub>2</sub>-free CO oxidation

Fig. 5 shows the full series of CO oxidation and PROX experiments for all the investigated samples. For each sample, the experiment consisted of a series of two CO oxidation heating/cooling cycles (“CO ox 1”), a reducing treatment, an additional series of two CO oxidation cycles (“CO ox 2”), and finally a series of two PROX cycles. For each couple of cycles, the reaction runs are numbered from 1 to 4 (see the scheme of Fig. 6 for the CO oxidation series).

While in the absence of H<sub>2</sub> the CO yield reaches 100% following the light-off period, the CO-PROX curves exhibit a sharp maximum (Fig. 5). This well-known behavior [8] is due to the adsorption competition between H<sub>2</sub> and CO (increasingly favorable to hydrogen as temperature increases, see the discussion on selectivity below) combined with the low availability of O<sub>2</sub> due to its reaction with CO and H<sub>2</sub>. Indeed, in each case the temperature of the maximum corresponds to the temperature at which O<sub>2</sub> is almost totally converted (Fig. S9).

<sup>2</sup> The CeOCl phase, characterized by an IR band a 2175 cm<sup>-1</sup> [49,50], was never detected in the samples prepared using Pt chloride.

The first heating run on the fresh samples prepared using nitrate precursor (Gly-N and ODH-N) shows higher CO oxidation activities than the three subsequent cycles (“CO ox 1” series), the temperature at half-conversion ( $T_{1/2}$ ) being afterwards shifted by more than +50 °C and stabilized from the second run. This effect is less pronounced for catalysts prepared using chloride precursor (Gly-Cl, Gly-Cl-w, and ODH-Cl). From the above conclusion of Raman and DRIFTS results, the initially high activity of the Gly-N and ODH-N samples can be related to the partial oxidation of Pt, whereas the other samples contain the less reactive stoichiometric PtO phase. This result is consistent with recent findings of Ke et al. showing that Pt clusters supported on ceria nanowires are more active for CO oxidation when the Pt-O coordination number is small [51].

The reducing treatment in H<sub>2</sub> flow at 400 °C has little effect on the subsequent CO oxidation activity (first run of “CO ox 2” series) of Gly samples, whereas a slight initial deactivation (Fig. 5d) or a significant activation (Fig. 5f) are observed for ODH catalysts. These results show a greater sensitivity of the latter to oxidizing/reducing conditions. Thus, it is likely that these two catalysts encounter restructuring upon thermal treatment at 400 °C. For the ODH-Cl catalyst (Fig. 5f), a further reducing treatment at 500 °C was attempted, but led to the same stabilized CO oxidation activity (Fig. S10, see Section 3.2.3).<sup>3</sup>

Whereas the SCS catalysts are stable or slightly regenerate/activate throughout the heating/cooling cycles (“CO ox 2” series), the Pt/CeO<sub>2</sub> sample prepared by IWI and submitted to a reducing pretreatment shows a marked activation during the same series,  $T_{1/2}$  decreasing overall by ca. 50 °C. This suggests that the Pt phase in SCS catalysts is stabilized in the post-reduction state, not only immediately after the reducing treatment but also after CO oxidation runs under CO:O<sub>2</sub> = 2:2 vol% conditions. Conversely, the IWI catalyst state is more sensitive to the temperature cycles.

Remarkably, the run-dependent  $T_{1/2}$  order seen in Fig. 5 is always the same for the “CO ox 1” series (run 1 < run 2 < run 4 < run 3) and the “CO ox 2” post-reduction series (run 2 < run 4 < run 3 < run 1), as illustrated in Fig. 6. Run 1 brings the catalyst near thermodynamic equilibrium with the reactive mixture and subsequent runs correspond to catalyst stabilization with small fluctuations due to variations in the redox nature of the mixture, which itself depends on the gaseous composition throughout the catalyst bed and on the reactor temperature. More precisely, the cycle sequence can be understood in terms of Pt oxidation degree, assuming that the most oxidized (fresh sample) state (CO ox 1, run 1) is always the most active and, consistently, the pre-reduced one (CO ox 2, run 1) is always the least active. Within the “CO ox 1” series, run 3 is always the least active one since the initially highly oxidized sample still had not reached its reduced state during the first cycle (runs 1 and 2). The difference between runs 2, 3 and 4 is small, corresponding to catalyst stabilization, but in general there still remains a small hysteresis (with  $T_{1/2}$  run 4 < run 3) consistent with the higher efficiency of more oxidized state. Indeed, the high-temperature part of run 3 corresponds to 100% CO conversion, *i.e.* oxygen-rich conditions. The behavior of the “CO ox 2” series after the first run can be understood in the same way, the order between runs 2, 3 and 4 being the same as that of the “CO ox 1” series. This explanation is consistent with the findings of Carlsson et al. [52] showing that, for a Pt/Al<sub>2</sub>O<sub>3</sub> catalyst, Pt oxidation and reduction steps must be added to the conventional Langmuir–Hinshelwood scheme to accurately describe the hysteresis observed during transient conditions. In addition, the authors evidence a highly reactive Pt<sup>δ+</sup> state in

<sup>3</sup> The ODH-N catalyst (Fig. 5d) contains poorly dispersed Pt particles (size 6.8 ± 3.8 nm, Table 1) and thus shows a lower PROX activity, with a maximum CO<sub>2</sub> yield of ca. 50% only.

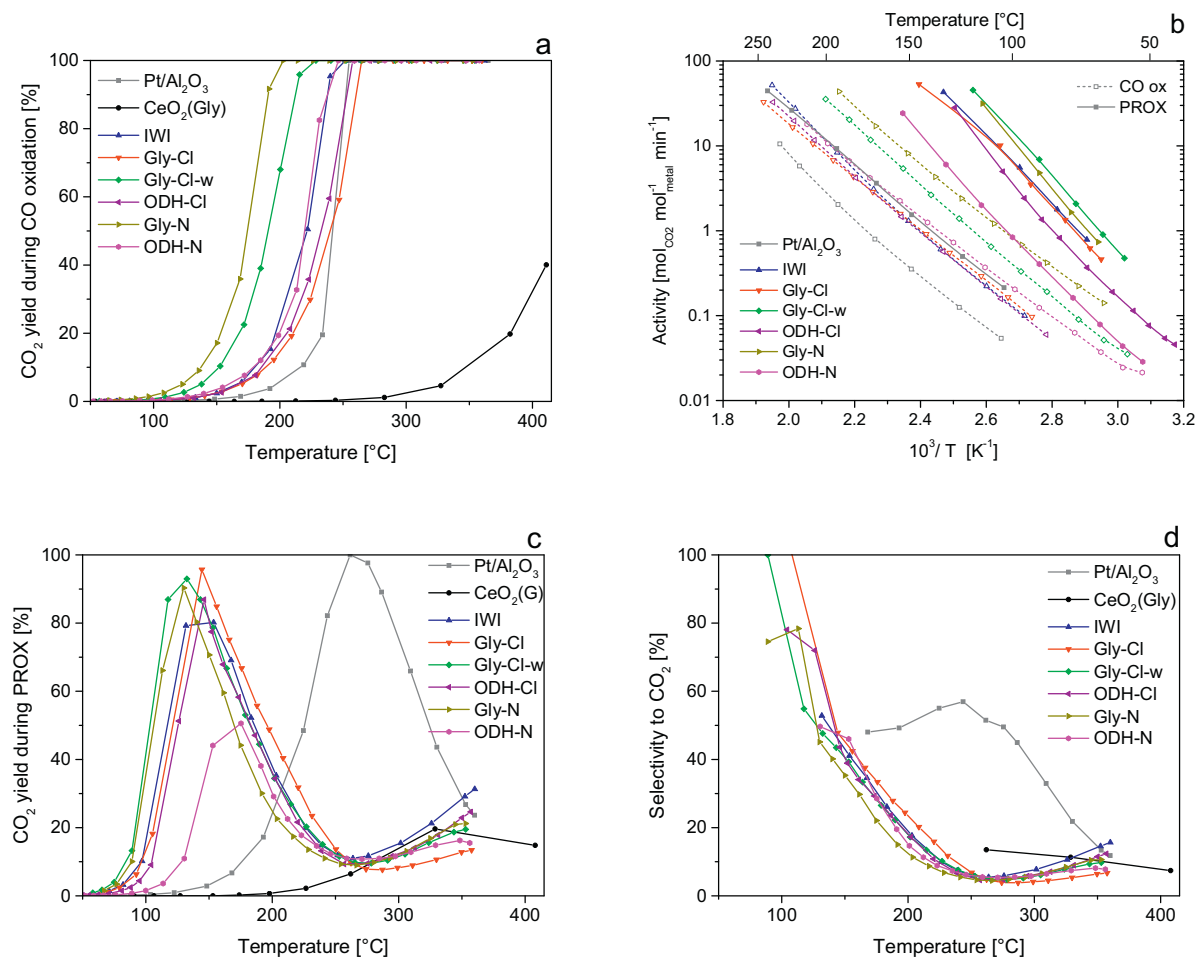


**Fig. 7.** Comparison of the catalyst performances (last reaction runs). (a) CO<sub>2</sub> yield versus temperature in CO oxidation. (b) Arrhenius plots of CO<sub>2</sub> formation rate in CO oxidation and PROX. (c) CO<sub>2</sub> yield versus temperature in PROX. (d) Selectivity to CO<sub>2</sub> in PROX.

oxidizing conditions, which reduces during the extinction process (corresponding to runs 2 and 4 in our case).

### 3.2.2. CO oxidation and PROX performances

Fig. 7 reports a comparison of the catalysts in terms of CO<sub>2</sub> yields (a and c), activities (b) and selectivities (d) for the last reaction runs. Fig. 8 shows in a simple manner the evolution of  $T_{1/2}$  from H<sub>2</sub>-free CO oxidation to CO PROX on all catalysts.

From Fig. 7a and c, bare ceria appears much less active in H<sub>2</sub>-free and H<sub>2</sub>-rich CO oxidation than the Pt-containing catalysts, which is well known [3,24]. According to the Arrhenius plot of Fig. 7b, the order of activity per mole of Pt for CO conversion is the following (see also Table 2).

CO oxidation : Pt/Al<sub>2</sub>O<sub>3</sub> << IWI ≈ ODH-Cl ≈ Gly-Cl ≤ ODH-N < Gly-Cl-w < Gly-N

COPROX : Pt/Al<sub>2</sub>O<sub>3</sub> << ODH-N << ODH-Cl < Gly-Cl ≈ IWI < Gly-N < Gly-Cl-w

The least active catalyst in both CO oxidation and PROX is Pt/Al<sub>2</sub>O<sub>3</sub>, confirming the promoting effect of ceria on active oxygen supply through the Mars van Krevelen's (redox) mechanism [5–8,24]. In this scheme [53] applied to our case, the key feature is the reaction at the ceria-Pt interface of labile oxygen from the ceria support with CO chemisorbed on platinum. The oxygen vacancy issuing from this process is then replenished either from adsorption of molecular O<sub>2</sub> at the interface or diffusion of a neighboring O atom.

The most active catalysts in both reactions are those prepared using glycine fuel, *i.e.* Gly-N and Gly-Cl-w Pt-CeO<sub>2</sub> samples. The ODH-Cl sample is among the least efficient catalysts because of its large amount of big Pt particles and/or its high content of residual chloride (0.53 wt%). Both reasons can actually be linked since Cl is known to favor metal nanoparticle sintering [54]. Consistently, the washing of Gly-Cl, which decreases the chloride amount by a factor of 3 (0.3 to 0.1 wt%), has a significant positive effect on the CO conversion activity (CO oxidation and PROX rates multiplied by *ca.* 3 at 110 °C, see Table 2). Indeed, the presence of Cl on ceria has been reported to inhibit the ceria-mediated reaction pathway [8,55]. The IWI (Cl) sample is comparatively more efficient for CO PROX than for H<sub>2</sub>-free CO oxidation, whereas the Cl-free

but poorly dispersed ODH-N catalyst shows the reverse trend. This can be understood in terms of (i) strong detrimental effect of Cl on CO oxidation and (ii) critical role of the Pt-ceria interface in PROX, as will be discussed in the next section. The Gly-Cl sample (prepared by one-pot combustion using glycine) and the IWI sample (prepared by impregnation of ceria combustion-synthesized using glycine), which contain similar amounts of chlorine, exhibit the same steady-state catalytic performances in both reactions. Hence, the preparation method has no influence on the results if

**Table 2**

Catalytic properties of the samples.

Sample name	$E_{app}$ CO ox. (kJ/mol) <sup>a</sup>	$E_{app}$ PROX (kJ/mol) <sup>a</sup>	Activity CO ox (min <sup>-1</sup> ) <sup>b</sup>	Activity PROX (min <sup>-1</sup> ) <sup>b</sup>	TOF CO ox. (min <sup>-1</sup> ) <sup>c</sup>	TOF PROX (min <sup>-1</sup> ) <sup>c</sup>
Pt/Al <sub>2</sub> O <sub>3</sub>	64.8 ± 1.9	62.3 ± 0.6	0.06	0.28	0.32	1.4
Pt/CeO <sub>2</sub> IWI (Cl)	68.0 ± 1.6	76.4 ± 1.3	0.20	12	0.65	40
Pt–CeO <sub>2</sub> Gly–Cl	58.8 ± 0.3	82.9 ± 1.9	0.24	13	1.1	59
Pt–CeO <sub>2</sub> Gly–Cl-w	64.2 ± 0.4	86.0 ± 1.4	0.72	33	2.5	112
Pt–CeO <sub>2</sub> ODH–Cl	63.1 ± 0.7	81.7 ± 2.4	0.20	7.6	1.2	43
Pt–CeO <sub>2</sub> Gly–N	58.8 ± 1.0	89.2 ± 1.4	1.5	25	6.2	105
Pt–CeO <sub>2</sub> ODH–N	56.7 ± 0.4	77.8 ± 1.3	0.36	1.8	3.6	18

<sup>a</sup> Apparent activation energy.<sup>b</sup> Activity at 110 °C in mol<sub>CO<sub>2</sub></sub> mol<sub>Pt</sub><sup>-1</sup> min<sup>-1</sup>.<sup>c</sup> Turnover frequency at 110 °C in mol<sub>CO<sub>2</sub></sub> mol<sub>Pt,surf</sub><sup>-1</sup> min<sup>-1</sup>.

we assume that all the Pt particles in the SCS sample are exposed to the gas phase. The XPS results of Fig. S8 confirm the similarity between these catalysts in terms of Pt oxidation state (88% of Pt<sup>0</sup> for both reduced samples), although the reduced IWI sample contains a greater fraction of Ce<sup>3+</sup> than the reduced SCS sample (25% vs. 12%).

In order to derive turnover frequencies (TOFs), the activities were normalized over the number of surface Pt atoms. To this purpose, for each sample the metal dispersion was calculated from  $1.1/\langle d \rangle_{surf}$ , where  $\langle d \rangle_{surf}$  is the surface-weighted mean particle diameter (Sauter diameter) in nm obtained from the particle size distribution [24,56] (see Table 1 and Fig. S6). The TOF values at 110 °C are reported in Table 2. Due to the moderate variation in Pt dispersion from a catalyst to another, the use of TOFs affects only slightly the hierarchy reported above in terms of CO oxidation activities.

Finally, Fig. 7d reports the catalyst selectivities for CO PROX. Strikingly, the values are similar for all the Pt–CeO<sub>2</sub> catalysts. In contrast to Pt/Al<sub>2</sub>O<sub>3</sub> showing a selectivity maximum of 57% at ca. 240 °C, the Pt–CeO<sub>2</sub> selectivity is 100% below ca. 100 °C and gradually decreases to less than 10% as the temperature increases to 250 °C, in agreement with the results of Wootsch et al. [8]. The intermediate temperature range reveals small differences between the catalysts, Gly–Cl and Gly–N being the most and least selective ones, respectively. This trend is consistent with the recent results of Jardim et al., who compared the PROX performances of Pt/CeO<sub>2</sub> catalysts prepared by impregnation using chloride and nitrate precursors [55]. Indeed, these authors measured a detrimental effect of chloride on CO PROX activity, and a benefit one on selectivity.

### 3.2.3. Effect of hydrogen on CO oxidation activity and mechanism

Fig. 8 focuses on the effect of H<sub>2</sub> on the temperature of half-CO-conversion ( $T_{1/2}$ ). Upon addition of 48 vol% H<sub>2</sub> in the reactant flow (PROX series), the temperature shifts to lower temperatures (by 60–120 °C) for all Pt–CeO<sub>2</sub> catalysts, with a CO oxidation activity multiplied by up to 60 at 110 °C (Table 2). As shown by Fig. 5, a gradual activation of the catalysts is observed, the first run showing limited promotion.<sup>4</sup> For Pt/Al<sub>2</sub>O<sub>3</sub>, the CO oxidation boost induced by H<sub>2</sub> is comparatively small ( $T_{1/2}$  decreases by 16 °C and the activity is multiplied by 4 at 110 °C).

The apparent activation energies ( $E_{app}$ ) of CO oxidation and PROX are reported in Table 2. For H<sub>2</sub>-free CO oxidation, the values for all the catalysts, including Pt/Al<sub>2</sub>O<sub>3</sub>, are similar (62 ± 4 kJ/mol). For PROX, whereas  $E_{app}$  is almost unchanged in the case of Pt/Al<sub>2</sub>O<sub>3</sub> (from 65 to 62 kJ/mol), it increases to 82 ± 5 kJ/mol for the Pt–CeO<sub>2</sub> catalysts. While it shows that the preparation parameters have little influence on the reaction mechanism, this result further underlines the crucial effect of ceria on the mechanistic change induced by H<sub>2</sub> for Pt-catalyzed CO oxidation.

Fig. S10 shows the results of PROX experiments performed at several concentrations of hydrogen (2%, 10%, and 48%). While the 2% hydrogen concentration leads to a modest rate enhancement, the maximum promotion is obtained from 10% H<sub>2</sub>. Such a boosting effect appears different from that observed for Au/Al<sub>2</sub>O<sub>3</sub>, on which (i) the CO oxidation rate is strongly enhanced by the introduction of even a very small amount of hydrogen (0.25%) in the reactant mixture, and (ii) for higher H<sub>2</sub> partial pressures (up to 75% H<sub>2</sub> concentration), the CO oxidation rate gradually increases with the hydrogen content [57]. Furthermore, in the case of Au/Al<sub>2</sub>O<sub>3</sub>, the apparent activation energy of CO oxidation is not or less affected by H<sub>2</sub> addition.

This promotion by H<sub>2</sub> cannot be due to: (i) a reducing effect of the H<sub>2</sub>-rich reactant mixture on Pt since the pretreatment at 400 °C under H<sub>2</sub> did not significantly boost the CO oxidation activity, as discussed in Section 3.2.1; (ii) a regeneration effect only because, in several cases (Cl samples, Fig. 5a,b and f), the first CO oxidation run shows lower activity than the CO PROX one; (iii) a direct benefit effect of water through the water-gas shift reaction [58,59]. Instead, as discussed in previous works on noble metals, the promoting effect of hydrogen could be ascribed to the formation of OOH reactive adspecies from reaction between O<sub>2</sub> and H<sub>2</sub> on the metal, as for Au catalysts [57–60] and/or to an H<sub>2</sub>-induced weakening of the CO–metal bond, as for Pt catalysts [59,61,62]. Given that this phenomenon was also observed in the case of unsupported metals [59,60,63], we suggest that for such non-reducible supports as Al<sub>2</sub>O<sub>3</sub> the promotion mechanism is intrinsic to the metal. However, since the promoting effect of H<sub>2</sub> is much more sig-

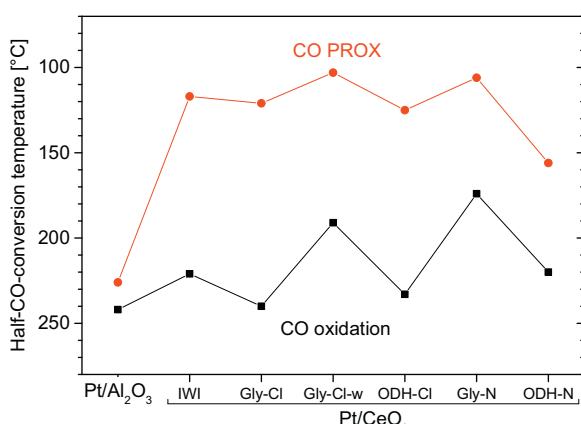


Fig. 8. Temperature of half-CO-conversion for CO oxidation (squares) and PROX (disks). With respect to Fig. 5, the last reaction runs have been considered.

<sup>4</sup> In the only case of ODH-Cl, a treatment (30 min at 120 °C) under an O<sub>2</sub> (2%) + H<sub>2</sub> (48%) reactive mixture was applied to the catalyst before PROX runs. This treatment leads to water formation and boosts the CO PROX activity, explaining why maximum activity is measured from the first PROX run for the ODH-Cl catalyst.

nificant for Pt/CeO<sub>2</sub> than for Pt/Al<sub>2</sub>O<sub>3</sub> and the apparent activation energy is modified only for ceria-supported catalysts, there exists an additional H<sub>2</sub> effect on Pt activity involving the ceria support. We propose that H<sub>2</sub> promotes CO oxidation by increasing the mobility of surface oxygen species from the ceria lattice, which are key intermediates in the Mars van Krevelen's mechanism. This may proceed directly through the formation of mobile and active O<sub>x</sub>H<sub>y</sub> intermediates or indirectly by the creation of oxygen vacancies (reduction), which themselves stimulate oxygen mobility. According to Duprez and coworkers, hydroxyl groups would facilitate the migration of oxygen species on ceria [8]. In all cases, hydrogen supply to ceria should be facilitated by H<sub>2</sub> dissociation on Pt nanoparticles followed by H spillover to the support, although low-temperature dissociation of H<sub>2</sub> on oxygen vacancies of pure ceria has also been reported [64].

Summarizing, in H<sub>2</sub>-free CO oxidation, the activity of Pt is strongly promoted by the ceria support (Fig. 8) provided that Cl does not poison the surface (as for IWI, Gly-Cl and ODH-Cl catalysts) and the number of Pt sites is not limited by a poor dispersion (ODH-N). In the presence of H<sub>2</sub> (PROX), in addition to the small intrinsic effect over Pt (as for Pt/Al<sub>2</sub>O<sub>3</sub>), a strong promoting effect of H<sub>2</sub> occurs via the ceria support, the rate becoming only determined by the supply of ceria O<sub>x</sub>H<sub>y</sub> species to the Pt particles. As chlorine decreases the number or mobility of such species and/or inhibits the formation of oxygen vacancies [8,55], the activity reached by chlorinated catalysts (IWI, Gly-Cl, ODH-Cl) is slightly inferior to that of washed (Gly-Cl-w) and Cl-free (Gly-N) ones, as shown by Fig. 8. Finally, given that the Pt particles of the ODH-N sample are bigger (7 nm in average diameter against 3–4 nm for other catalysts), the CO PROX activity of this catalyst is limited by the number of Pt-ceria interfacial sites.

#### 4. Conclusions

Pt–CeO<sub>2</sub> catalysts were prepared by SCS using two types of fuels (glycine or ODH) and Pt precursors (chloride or nitrate). To our knowledge, the fuel effect in SCS had never been reported for noble metal-ceria systems. These catalysts were tested and compared to bare CeO<sub>2</sub>, impregnated Pt/CeO<sub>2</sub> and Pt/Al<sub>2</sub>O<sub>3</sub> for CO oxidation (CO:O<sub>2</sub> = 2:2 mol%) and PROX (CO:O<sub>2</sub>:H<sub>2</sub> = 2:2:48 mol%) using heating/cooling temperature cycles in a flow-fixed-bed reactor.

Although the fuel type significantly affects the ceria texture and microstructure, Pt nanoparticles of 3–4 nm in size are generally obtained from SCS. Raman and infrared spectroscopies revealed that the fresh SCS catalysts prepared using chloride precursor exhibit PtO particles whereas their nitrate counterparts only contain Pt<sup>δ+</sup> species in interaction with ceria. The difference in Pt oxidation state was ascribed to the relative stabilities of the two metal precursors. As the Cl-free catalysts are initially much more active than the Cl-containing or prereduced ones for CO adsorption and oxidation, we concluded that the most active state is Pt<sup>δ+</sup>. After stabilization throughout CO oxidation cycles, analysis of the slight hysteresis remaining in the CO conversion curves again evidenced that the activity is always favored by a positive oxidation state of Pt (provided that no bulk oxide is formed).

Comparison of the stabilized H<sub>2</sub>-free CO oxidation and PROX performances of the Pt-based catalysts showed that both the presence of ceria (instead of alumina) and the absence of chlorine promote both reactions. However, the poisoning by Cl is more detrimental for CO oxidation than for PROX. The most efficient catalysts are those synthesized by combustion using glycine fuel combined either with Pt nitrate precursor or Pt chloride followed by Cl washing. However, the selectivity to CO<sub>2</sub>, which is 100% and gradually decreases above ca. 100 °C, is similar for all Pt–CeO<sub>2</sub> catalysts, including the one prepared by impregnation.

Importantly, the addition of hydrogen in the CO–O<sub>2</sub> feed for PROX induces a strong enhancement of the CO oxidation activity of the Pt–CeO<sub>2</sub> catalysts, the light-off temperature decreasing by up to 120 °C. For Pt/Al<sub>2</sub>O<sub>3</sub>, the effect is smaller and does not involve the support. We suggested that hydrogen, by increasing the mobility of lattice oxygen or oxygen-containing species such as OH groups at the surface of ceria, reinforces the ceria-mediated reaction pathway of CO oxidation. As a result, the CO conversion rate is no longer determined by active oxygen supply but rather by CO + O reaction at the Pt-ceria interface, as recently suggested by our comparison of Pt-group metals [24]. Cl ions, which inhibit oxygen diffusion on ceria and poison Pt sites, have a slight detrimental effect on CO PROX.

#### Acknowledgements

LP thanks Stéphane Lordinat for fruitful discussions on Raman data. Mimoun Aouine (TEM), Laurence Burel (SEM), Françoise Bosselet (XRD), Luis Cardenas (XPS), Noëlle Cristin and Pascale Mascunian (ICP) are greatly acknowledged for sample analyses and related discussions. The CLYM is acknowledged for access to the FEI Titan microscope, and the European COST Action CM1104 "Red ox" for networking discussions.

#### Appendix A. Supplementary data

Supplementary data associated with this article can be found, in the online version, at <http://dx.doi.org/10.1016/j.apcatb.2016.01.056>.

#### References

- [1] N. Bion, F. Epron, M. Moreno, F. Mariño, D. Duprez, *Top. Catal.* 51 (2008) 76–88.
- [2] E.D. Park, D. Lee, H.C. Lee, *Catal. Today* 139 (2009) 280–290.
- [3] K. Liu, A. Wang, T. Zhang, *ACS Catal.* 2 (2012) 1165–1178.
- [4] A. Trovarelli, P. Fornasiero, *Catalysis by Ceria and Related Materials*, 2nd edition, Imperial College Press, 2013.
- [5] T. Baulnes, E.S. Putna, R.J. Gorte, *Catal. Lett.* 41 (1996) 1–5.
- [6] F. Mariño, C. Descorme, D. Duprez, *Appl. Catal. B* 54 (2004) 59–66.
- [7] Y. Huang, A. Wang, X. Wang, T. Zhang, *Int. J. Hydrogen Energy* 32 (2007) 3880–3886.
- [8] A. Wootsch, C. Descorme, D. Duprez, *J. Catal.* 225 (2004) 259–266.
- [9] S.L. González-Cortés, F.E. Imbert, *Appl. Catal. A* 452 (2013) 117–131.
- [10] P. Bera, K.C. Patil, V. Jayaram, G.N. Subbanna, M.S. Hegde, *J. Catal.* 196 (2000) 293–301.
- [11] P. Bera, K.R. Priolkar, A. Gayen, P.R. Sarode, M.S. Hegde, S. Emura, R. Kumashiro, V. Jayaram, G.N. Subbanna, *Chem. Mater.* 15 (2003) 2049–2060.
- [12] P. Bera, A. Gayen, M.S. Hegde, N.P. Lalla, L. Spadaro, F. Frusteri, F. Arena, *J. Phys. Chem. B* 107 (2003) 6122–6130.
- [13] M.S. Hegde, P. Bera, *Catal. Today* 253 (2015) 40–50.
- [14] L. Pino, A. Vita, F. Cipiti, M. Lagana, V. Recupero, *Appl. Catal. A* 306 (2006) 68–77.
- [15] U.-S. Amjad, A. Vita, C. Galletti, L. Pino, S. Specchia, *Ind. Eng. Chem. Res.* 52 (2013) 15428–15436.
- [16] A. Vita, G. Cristiano, C. Italiano, L. Pino, S. Specchia, *Appl. Catal. B* 162 (2015) 551–563.
- [17] S. Colussi, A. Gayen, M. Farnesi Camellone, M. Boaro, J. Llorca, S. Fabris, A. Trovarelli, *Angew. Chem. Int. Ed.* 48 (2009) 8481–8484.
- [18] A. Gayen, M. Boaro, C. de Leitenburg, J. Llorca, A. Trovarelli, *J. Catal.* 270 (2010) 285–298.
- [19] S. Colussi, A. Gayen, J. Llorca, C. de Leitenburg, G. Dolcetti, A. Trovarelli, *Ind. Eng. Chem. Res.* 51 (2012) 7510–7517.
- [20] S. Colussi, A. Gayen, M. Boaro, J. Llorca, A. Trovarelli, *ChemCatChem* 7 (2015) 2222–2229.
- [21] A.I. Boronin, E.M. Slavinskaya, I.G. Danilova, R.V. Gulyaev, Y.I. Amosov, P.A. Kuznetsov, I.A. Polukhina, S.V. Koscheev, V.I. Zaikovskii, A.S. Noskov, *Catal. Today* 144 (2009) 201–211.
- [22] T.-S. Nguyen, G. Postole, S. Lordinat, F. Bosselet, L. Burel, M. Aouine, L. Massin, F. Morfin, P. Gélin, L. Piccolo, *J. Mater. Chem. A* 2 (2014) 19822–19832.
- [23] G. Postole, T.-S. Nguyen, M. Aouine, P. Gélin, L. Cardenas, L. Piccolo, *Appl. Catal. B* 166–167 (2015) 580–591.
- [24] T.-S. Nguyen, F. Morfin, M. Aouine, F. Bosselet, J.-L. Rousset, L. Piccolo, *Catal. Today* 253 (2015) 106–114.
- [25] A. Kaftan, F. Kolhoff, T.S. Nguyen, L. Piccolo, M. Laurin, J. Libuda, *Catal. Sci. Technol.* (2016), <http://dx.doi.org/10.1039/C5CY00827A>.

[26] S.R. Jain, K.C. Adiga, V.R. Pai Verneker, *Combust. Flame* 40 (1981) 71–79.

[27] K.S.W. Sing, D.H. Everett, R.A.W. Haul, L. Moscou, R.A. Pierotti, J. Rouquérol, T. Siemieniewska, *Pure Appl. Chem.* 57 (1985) 603–619.

[28] S. Alayoglu, K. An, G. Melaet, S. Chen, F. Bernardi, L.W. Wang, A.E. Lindeman, N. Musselwhite, J. Guo, Z. Liu, M.A. Marcus, G.A. Somorjai, *J. Phys. Chem. C* 117 (2013) 26608–26616.

[29] X.-D. Zhou, W. Huebner, *Appl. Phys. Lett.* 79 (2001) 3512–3514.

[30] W.H. Weber, K.C. Hass, J.R. McBride, *Phys. Rev. B* 48 (1993) 178–185.

[31] A. Nakajima, A. Yoshihara, M. Ishigame, *Phys. Rev. B* 50 (1994) 13297–13307.

[32] J.E. Spanier, R.D. Robinson, F. Zhang, S.-W. Chan, I.P. Herman, *Phys. Rev. B* 64 (2001) 245407.

[33] M. Daniel, S. Lomidant, *J. Raman Spectrosc.* 43 (2012) 1312–1319.

[34] Z.D. Dohčević-Mitrović, M.J. Šćepanović, M.U. Grujić-Brojčin, Z.V. Popović, S.B. Bošković, B.M. Matović, M.V. Zinkevich, F. Aldinger, *Solid State Commun.* 137 (2006) 387–390.

[35] G. Gouadec, P. Colombari, *Prog. Cryst. Growth Charact. Mater.* 53 (2007) 1–56.

[36] V. Grover, A. Banerji, P. Sengupta, A.K. Tyagi, *J. Solid State Chem.* 181 (2008) 1930–1935.

[37] I. Kosacki, T. Suzuki, H.U. Anderson, P. Colombari, *Solid State Ionics* 149 (2002) 99–105.

[38] M.S. Brogan, T.J. Dines, J.A. Cairns, *J. Chem. Soc. Faraday Trans.* 90 (1994) 1461–1466.

[39] W. Lin, A.A. Herzing, C.J. Kiely, I.E. Wachs, *J. Phys. Chem. C* 112 (2008) 5942–5951.

[40] J.R. McBride, G.W. Graham, C.R. Peters, W.H. Weber, *J. Appl. Phys.* 69 (1991) 1596–1604.

[41] G.I.N. Waterhouse, G.A. Bowmaker, J.B. Metson, *Phys. Chem. Chem. Phys.* 3 (2001) 3838–3845.

[42] L.L. Murrell, S.J. Tauster, D.R. Anderson, *Stud. Surf. Sci. Catal.* 71 (1991) 275–289.

[43] J.R. McBride, K.C. Hass, B.D. Poindexter, W.H. Weber, *J. Appl. Phys.* 76 (1994) 2435.

[44] T. Shishido, H. Nasu, L. Deng, K. Teramura, T. Tanaka, *J. Phys. Conf. Ser.* 430 (2013) 012060.

[45] T. Jin, Y. Zhou, G.J. Mains, J.M. White, *J. Phys. Chem.* 91 (1987) 5931–5937.

[46] D.W. Daniel, *J. Phys. Chem.* 92 (1988) 3891–3899.

[47] A. Holmgren, B. Andersson, D. Duprez, *Appl. Catal. B* 22 (1999) 215–230.

[48] P. Bazin, O. Saur, J.C. Lavalle, M. Daturi, G. Blanchard, *Phys. Chem. Chem. Phys.* 7 (2005) 187–194.

[49] L. Kępiński, J. Okal, *J. Catal.* 192 (2000) 48–53.

[50] A. Badri, C. Binet, J.-C. Lavalle, *J. Phys. Chem.* 100 (1996) 8363–8368.

[51] J. Ke, W. Zhu, Y. Jiang, R. Si, Y.-J. Wang, S.-C. Li, C. Jin, H. Liu, W.-G. Song, C.-H. Yan, Y.-W. Zhang, *ACS Catal.* 5 (2015) 5164–5173.

[52] P.-A. Carlsson, L. Österlund, P. Thormählen, A. Palmqvist, E. Fridell, J. Jansson, M. Skoglundh, *J. Catal.* 226 (2004) 422–434.

[53] P. Mars, D.W. van Krevelen, *Chem. Eng. Sci.* 1 (Suppl. 3) (1954) 41–59.

[54] Z.C. Zhang, B.C. Beard, *Appl. Catal. A* 188 (1999) 229–240.

[55] E.O. Jardim, S. Rico-Francés, F. Coloma, J.A. Anderson, J. Silvestre-Albero, A. Sepúlveda-Escribano, *J. Colloid Interface Sci.* 443 (2015) 45–55.

[56] L. Piccolo, S. Nassreddine, M. Aouine, C. Ulhaq, C. Geantet, *J. Catal.* 292 (2012) 173–180.

[57] E. Quinet, F. Morfin, F. Diehl, P. Avenier, V. Caps, J.-L. Rousset, *Appl. Catal. B* 80 (2008) 195–201.

[58] E. Quinet, L. Piccolo, F. Morfin, P. Avenier, F. Diehl, V. Caps, J.-L. Rousset, *J. Catal.* 268 (2009) 384–389.

[59] L. Piccolo, S. Nassreddine, F. Morfin, *Catal. Today* 189 (2012) 42–48.

[60] T. Déronzier, F. Morfin, L. Massin, M. Lomello, J.-L. Rousset, *Chem. Mater.* 23 (2011) 5287–5289.

[61] J.L. Ayastuy, A. Gil-Rodríguez, M.P. González-Marcos, M.A. Gutiérrez-Ortiz, *Int. J. Hydrol. Energy* 31 (2006) 2231–2242.

[62] S. Salomons, R.E. Hayes, M. Votsmeier, *Appl. Catal. A* 352 (2009) 27–34.

[63] E. Quinet, L. Piccolo, H. Daly, F.C. Meunier, F. Morfin, A. Valcarcel, F. Diehl, P. Avenier, V. Caps, J.-L. Rousset, *Catal. Today* 138 (2008) 43–49.

[64] S.M. Schimming, G.S. Foo, O.D. LaMont, A.K. Rogers, M.M. Yung, A.D. D'Amico, C. Sievers, *J. Catal.* 329 (2015) 335–347.